



HAL
open science

Current and optimal dimensions predictions for a porous micro-electrode

Tien Dung Le, Didier Lasseux

► **To cite this version:**

Tien Dung Le, Didier Lasseux. Current and optimal dimensions predictions for a porous micro-electrode. ChemElectroChem, 2020, 10.1002/celc.202000508 . hal-02604596v1

HAL Id: hal-02604596

<https://hal.science/hal-02604596v1>

Submitted on 16 May 2020 (v1), last revised 6 Sep 2022 (v2)

HAL is a multi-disciplinary open access archive for the deposit and dissemination of scientific research documents, whether they are published or not. The documents may come from teaching and research institutions in France or abroad, or from public or private research centers.

L'archive ouverte pluridisciplinaire **HAL**, est destinée au dépôt et à la diffusion de documents scientifiques de niveau recherche, publiés ou non, émanant des établissements d'enseignement et de recherche français ou étrangers, des laboratoires publics ou privés.

1 Current and optimal dimensions predictions for a
2 porous micro-electrode

3 Tien D. Le ^{*†} Didier Lasseux^{‡*}

4 **1 Abstract**

5 The expression of the current delivered by a cylindrical porous micro-electrode
6 operating a single heterogeneous reaction and mass diffusion of the reagent is
7 analytically derived in this work from a *complete solution* of the diffusion/reaction
8 macroscopic problem. This solution is valid regardless of the aspect (thickness
9 to inner radius) ratio. It encompasses the *hybrid solution* reported elsewhere,
10 valid only when this ratio remains small compared to unity, and, consequently,
11 the case of a planar electrode as well. The asymptotic form of the solution in
12 this latter case is also provided. The complete solution is used to predict the
13 optimal thickness of the electrode and its optimal inner radius (*i.e.* the sup-
14 porting wire radius) corresponding to the best compromise between a minimum
15 electrode volume and a maximum current **per unit volume**. This work hence
16 provides a complete optimization procedure that can be used as predictive tools
17 for the design of porous electrodes.

18 **2 Introduction**

19 The development of miniaturized electrodes has been the subject of intense in-
20 terest for the past decade, in particular for bio-implantable electro-devices (see²⁶
21 and references therein). In order to reduce their size, micro- or nanoporous ma-
22 terials are particularly attractive due to their high specific surface area available
23 for the **heterogeneous** redox reactions, hence producing a much larger current
24 than a flat electrode of the same size²³. An abundant literature has been ded-
25 icated to the study of these devices, both from theoretical and experimental
26 points of view. Many different operating conditions can be envisaged for these
27 electrodes^{17;5;21;9}, namely without any catalyst^{13;15} or with an embedded en-
28 zyme to catalyze the redox reactions which may occur in the **direct electron**
29 **transfer**^{7;14} or **mediated electron transfer** mode⁶. A classical procedure to obtain

*I2M, UMR 5295, CNRS, Univ. Bordeaux, Esplanade des Arts et Métiers, 33405 Talence
CEDEX, France

†Université de Lorraine, CNRS, LEMTA, F-54000 Nancy, France

‡corresponding author

30 a porous material relies on a Langmuir-Blodgett templating method related to
31 self-assembly of particles. This is followed by electrodeposition of a conducting
32 material. After dissolving the particles, a synthetic porous electrode composed
33 of interconnected pores is obtained which porosity and internal architecture can
34 be tuned^{20;12;23}.

35 The coupled process of transport and electrochemical reaction occurring dur-
36 ing voltammetry experiments for porous electrodes has been modelled in both
37 cases with or without catalysis^{18;1;2}. Recently, a multiscale model for a porous
38 electrode operating a single reaction was developed¹³, providing a macroscopic
39 model and a closure problem which solution allows to determine the effective pa-
40 rameter (effective diffusion coefficient). Such a model was validated by compar-
41 ing its predictions with 3D direct numerical simulations at the pore scale **similar**
42 **to those reported recently?**. It was also successfully compared with experimen-
43 tal data. **The advantage of such an approach is that the ensuing macroscale**
44 **model, which contains the necessary information from the microscale, is much**
45 **simpler to solve than the original one at the scale of the microstructure, avoiding**
46 **cumbersome direct numerical simulations at this scale.** Further, an optimization
47 procedure, based on the macroscopic model to estimate the optimal thickness of
48 cylindrical porous electrodes, has been investigated¹⁶. It was derived under the
49 assumption that the electrode thickness is much smaller than its inner radius,
50 although the diffusion layer thickness surrounding the electrode is not. This
51 yielded the so-called *hybrid model*. However, such an assumption can fail in
52 practice and it is hence of major interest to derive a prediction of the optimal
53 thickness in the general case.

54 In the present work, an accurate *complete solution* of the upscaled model
55 **in its general form** is proposed in order to predict the current delivered by a
56 cylindrical electrode in the steady regime and to estimate its optimal thickness
57 **and optimal inner radius** without any assumption on its **microstructure** and
58 **dimensions. This solution is expressed in terms of the Bessel's functions of the**
59 **first and second kinds; it is valid whatever the thickness to inner radius ratio**
60 **and is hence general.**

61 Predictions of this model are compared to those obtained from the hybrid
62 model in the case of a face-centered cubic, cubic and body-centered cubic struc-
63 tures of the porous material. Moreover, an analytical solution is also derived for
64 planar electrodes which conveniently matches the complete solution for cylindri-
65 cal electrodes in the limit of an extremely large radius compared to the thickness.
66 Finally, the optimal radius of the supporting wire that leads to the minimum
67 volume of the electrode is derived. This represents a very important result,
68 leading to a complete optimization process of the macroscopic dimensions of
69 the electrode.

70 The paper is organized as follows. In Section 2, the upscaled model for the
71 coupled electrochemical reaction and transport in a porous micro-electrode is
72 briefly recalled. A complete analytical solution of the macroscopic model for
73 a cylindrical geometry is proposed in Section 3 without any restriction on the
74 electrode dimensions. Such a solution is compared to that of the hybrid model
75 developed in¹⁶ to predict the optimal electrode thickness. In Section 4, an

76 analytical solution of the macroscopic model and for the optimal thickness of
 77 a planar electrode is proposed. Section 5 is dedicated to the derivation of the
 78 optimal radius of the cylindrical wire supporting the electrode, which, along
 79 with its optimal thickness, provides a complete framework for its macroscopic
 80 optimization. Concluding remarks are drawn in Section 6.

81 3 Recall of the upscaled model

In this section, the upscaled model for a porous electrode operating a single reduction reaction, as proposed in previous works^{13;16}, is briefly recalled to further develop its solution. This model is derived from the pore-scale initial boundary value problem (IBVP) describing the coupled diffusion and heterogeneous reaction of the species of interest. Diffusion of this species, A , (of molar concentration c_A) dissolved in the solution saturating the electrode's pore space, denoted Ω_f , is governed by Fick's law⁸. It is beyond the scope of this article to provide the details for this governing law to apply here. The reader is referred to²⁵ for the assumptions and constraints that support it. At the pore solid/fluid interfaces, \mathcal{I}_{sf} , a single reaction reducing A to B is considered for which the electron transfer mechanism is described by the Butler-Volmer's relation³ (see Fig. 1). The IBVP at the pore scale can be formulated as follows

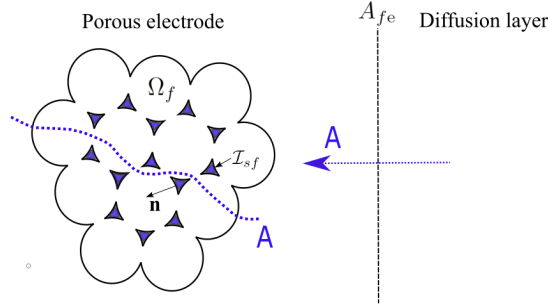


Figure 1 – Pore-scale configuration.

$$\frac{\partial c_A}{\partial t} = \nabla \cdot (\mathcal{D}_A \nabla c_A) \quad \text{in } \Omega_f \quad (1a)$$

$$\text{B.C.1} \quad -\mathbf{n} \cdot \mathcal{D}_A \nabla c_A = k_0 \alpha_A c_A \quad \text{at } \mathcal{I}_{sf} \quad (1b)$$

$$\text{B.C.2} \quad c_A = \mathcal{G}_A(\mathbf{r}, t) \quad \mathbf{r} \in A_{fe}, \forall t \quad (1c)$$

$$\text{I.C.} \quad c_A = \mathcal{F}_A(\mathbf{r}) \quad \mathbf{r} \in \Omega_f, t = 0 \quad (1d)$$

82 In these equations, \mathcal{D}_A is the molecular diffusion coefficient of species A , \mathbf{n}
 83 denotes the unit normal vector at \mathcal{I}_{sf} , pointing out of Ω_f , and k_0 is the standard
 84 rate constant of the reaction. Moreover, $\alpha_A = \exp\left(\frac{-\alpha n F (E - E^0)}{RT}\right)$ where α ,
 85 n , E and E^0 are the electron transfer coefficient, the number of transferred

86 electrons, the electrode potential and the standard potential respectively, F , R
 87 and T representing the Faraday's constant, ideal gas constant and temperature.
 88 In this work, T is assumed to be constant and the conduction of electrons in the
 89 solid phase is supposed to be extremely fast so that the potential in this phase
 90 can be readily considered as uniform. It should be noted that in the boundary
 91 condition B.C.2, $A_{fe} = \Omega_f \cap \Omega_e$ is the entrance and/or exit boundaries of the
 92 fluid phase, Ω_f , from/into the diffusion layer surrounding the electrode, denoted
 93 Ω_e .

The above pore-scale IBVP can be upscaled using the volume averaging method²⁴ to obtain a model at the macroscopic scale. To do so, a separation of length-scales is assumed between the characteristic pore length-scale, ℓ_p , and the characteristic macroscopic length scale, L , of the system. In addition, it is assumed that an intermediate scale r_0 can be exhibited satisfying $\ell_p \ll r_0 \ll L$ such that an averaging domain, \mathbf{V} , of measure V and size r_0 can be used to average the pore-scale IBVP. The domain \mathbf{V} is usually chosen so as to contain all the necessary microstructural information in order to be a **representative elementary volume** (REV) of the porous medium and the physical process at play. In this way, the macroscopic model is expressed in terms of the intrinsic average concentration of species A , denoted $\langle c_A \rangle^f$. It is defined in \mathbf{V} in which the fluid phase occupies a domain \mathbf{V}_f , of measure V_f , as

$$\langle c_A \rangle^f = \frac{1}{V_f} \int_{\mathbf{V}_f(\mathbf{x})} c_A dV \quad (2)$$

The averaging procedure is then carried out in three main steps. The averaging operator of Eq. (2) is first applied to the pore-scale IBVP, and in order to interchange time and space derivations with integration, the general transport theorem²² and the averaging theorem¹¹ are employed. When the porous medium is rigid and homogeneous, they can be respectively expressed as

$$\left\langle \frac{\partial \psi}{\partial t} \right\rangle^f = \frac{\partial \langle \psi \rangle^f}{\partial t} \quad (3a)$$

$$\langle \nabla \psi \rangle^f = \nabla \langle \psi \rangle^f + \frac{1}{V_f} \int_{\mathcal{A}_{sf}} \mathbf{n} \psi dA \quad (3b)$$

94 In the latter, \mathcal{A}_{sf} , of measure A_{sf} , represents the portion of \mathcal{I}_{sf} contained in \mathbf{V} .
 95 In a second step, the physical variables ψ (here $\psi = c_A$) are spatially decomposed
 96 under the form $\psi = \langle \psi \rangle^f + \tilde{\psi}$ ¹⁰, $\tilde{\psi}$ representing the spatial fluctuations of ψ with
 97 respect to its average $\langle \psi \rangle^f$. This decomposition is introduced in the averaged
 98 equations which can be usually simplified on the basis of the scale hierarchy.
 99 This yields an unclosed model in which both $\langle \psi \rangle^f$ and $\tilde{\psi}$ are present. In a
 100 third step, the (initial) boundary value problem for $\tilde{\psi}$ is derived and this is
 101 obtained by subtracting the unclosed macroscopic equations from their pore-
 102 scale analogues. The equations for $\tilde{\psi}$ are then simplified on the basis of the
 103 length scale constraints. These constraints further allow obtaining a formal

104 solution expressed in terms of *closure variables* by making the problem on $\tilde{\psi}$
 105 periodic over a periodic unit cell, at least as large as the REV. For simplicity,
 106 this periodic unit cell is identified as the REV in the remainder of this work.
 107 The formal solution for $\tilde{\psi}$ is introduced in the unclosed macroscopic equations,
 108 on the one hand, and in the problem for $\tilde{\psi}$, on the other hand, yielding the
 109 closed macroscopic model and the *closure problem(s)* for the closure variables,
 110 respectively. The closed model involves effective coefficients that are determined
 111 from the solution of the closure problem(s).

112 When the procedure described above is applied to the IBVP in Eqs. (1), the
 113 following macroscopic mass conservation equation is obtained^{13;16}

$$\epsilon_f \frac{\partial \langle c_A \rangle^f}{\partial t} = \nabla \cdot \left(\epsilon_f \mathbf{D}_{eff} \cdot \nabla \langle c_A \rangle^f \right) - k_0 \alpha_A a_v \langle c_A \rangle^f \quad \text{in } \Omega \quad (4)$$

Here, Ω denotes the macroscopic domain occupied by the electrode whereas ϵ_f
 and a_v are the porosity and specific area, respectively defined by

$$\epsilon_f = \frac{V_f}{V}; \quad a_v = \frac{A_{sf}}{V} \quad (5)$$

In addition, in Eq. (4), \mathbf{D}_{eff} is the effective diffusion tensor which is computed
 from the solution of an intrinsic closure problem in a periodic REV (see Eqs.
 (16) reported in a previous work¹³). An example of a REV, of size $\ell_R \equiv r_0$,
 is depicted in Fig. 2 for a FCC structure constitutive of a porous electrode. It

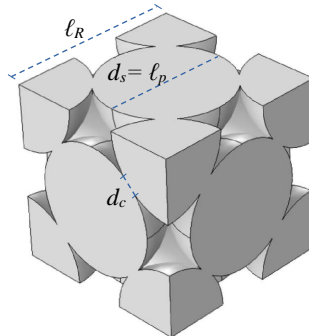


Figure 2 – Unit cell of a FCC structure with the characteristic dimensions. The gray area corresponds to the fluid domain while the solid phase is not represented. Spherical pores are connected through windows of diameter d_c .

should be noted that the second term on the right hand side of Eq. (4) originates
 from the heterogeneous reduction reaction of species A indicated in the pore-
 scale boundary condition in Eq. (1b) that is now reflected in the macroscopic
 mass conservation equation. The current delivered by the electrode can then be
 expressed from the average concentration as¹³

$$I = -nk_0 F \alpha_A a_v \int_{\Omega} \langle c_A \rangle^f dV \quad (6)$$

114 To obtain the solution on $\langle c_A \rangle^f$ in Ω , macroscopic boundary and initial con-
 115 ditions corresponding to the pore-scale analogues in Eqs. (1c) and (1d) must be
 116 specified. In practice, the electrode is immersed in the fluid saturating the pores.
 117 The mass transfer of species A in the surrounding bulk fluid, which is assumed
 118 to obey Fick's second law (Eq. (1a)), gives rise to a diffusion layer, of thickness
 119 L_N , next to the fluid-electrode boundary. The concentration at the outer edge
 120 of this boundary layer remains constant over time and is denoted c_A^0 which is
 121 assumed to be the uniform concentration value in the whole system at $t = 0$. At
 122 the boundary between the electrode and the diffusion layer, continuity of both
 123 the concentration and the flux can be reasonably assumed as was investigated
 124 earlier¹³ Appendix B. A resistance to mass transfer may be considered at the
 125 fluid-electrode boundary. However, this mechanism would contribute to hinder
 126 the penetration of species A inside the electrode and would hence lead to predict
 127 an optimal thickness smaller than that in the absence of this mechanism. In the
 128 following the existence of mass transfer resistance is ignored with the idea that
 129 this leads to the maximum expected value of the optimal electrode thickness.
 130 Moreover, in order to determine this optimal thickness, the stationary regime
 131 is to be considered for which the penetration depth of the diffusion/reaction
 132 front has settled down inside the electrode.

133 The solution of the coupled diffusion-reaction macroscopic equation (4), con-
 134 sidering the diffusion layer in the bulk fluid next to Ω , was proposed for a cylin-
 135 drical electrode in the stationary regime¹⁶. However, this solution was restricted
 136 to the case where the thickness of the electrode remains small compared to its
 137 inner radius, although this assumption may not apply to the outer boundary
 138 layer thickness. This led to a so-called hybrid model. In practice, the electrode
 139 can be thick enough for this assumption to fail and it is hence of major impor-
 140 tance to reconsider the problem in a more general case by deriving a solution
 141 referred to as the complete solution (or *Bessel's solution*). This is the purpose
 142 of the following section.

143 4 Cylindrical electrode

144 The cylindrical electrode under consideration is made of a porous material de-
 145 posited on a conducting cylindrical wire of radius R_1 . Its thickness is L_e and
 146 its external radius $R_2 = R_1 + L_e$. The diffusion layer outside the electrode is
 147 supposed to have an external radius $R_3 = R_2 + L_N$. A schematic cross section of
 148 the configuration, with the normalized characteristic radial dimensions denoted
 149 with the superscript $*$, is depicted in Fig. 3. The reference dimension used to
 150 normalize the radial coordinate is the characteristic size, ℓ_R , of the periodic unit
 151 cell (the REV) of the porous medium. The wire center is positioned at $r^* = 0$.

Using the initial concentration c_A^0 , that is supposed to be uniform in the
 whole system at $t = 0$, as the reference concentration, and assuming that steady

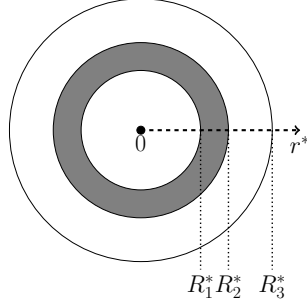


Figure 3 – Cross section of a cylindrical electrode of external dimensionless radius R_2^* made of a porous material (gray area) deposited on a cylindrical wire of dimensionless radius R_1^* and surrounded by the diffusion layer which external dimensionless radius is R_3^* .

state is reached, the macroscale problem takes the following form

$$r^{*2} \frac{d^2 \langle c_A^* \rangle^f}{dr^{*2}} + r^* \frac{d \langle c_A^* \rangle^f}{dr^*} = \varphi^2 r^{*2} \langle c_A^* \rangle^f \quad R_1^* \leq r^* \leq R_2^* \quad (7a)$$

$$\frac{d}{dr^*} \left(r^* \frac{dc_A^*}{dr^*} \right) = 0 \quad R_2^* \leq r^* \leq R_3^* \quad (7b)$$

$$\text{B.C.1: } D_{eff}^* \frac{d \langle c_A^* \rangle^f}{dr^*} = \frac{dc_A^*}{dr^*} \quad r^* = R_2^* \quad (7c)$$

$$\text{B.C.2: } \langle c_A^* \rangle^f = c_A^* \quad r^* = R_2^* \quad (7d)$$

$$\text{B.C.3: } \frac{d \langle c_A^* \rangle^f}{dr^*} = 0 \quad r^* = R_1^* \quad (7e)$$

$$\text{B.C.4: } c_A^* = 1 \quad r^* = R_3^* \quad (7f)$$

In B.C.1 and B.C.2, continuity of both the flux and the concentration is assumed at the porous electrode-diffusion layer interface ($r^* = R_2^*$). At the electrode-wire interface, $r^* = R_1^*$, a zero flux is considered whereas a Dirichlet boundary condition is used at the external boundary of the diffusion layer ($r^* = R_3^*$) where the initial concentration, c_A^0 , is imposed. In Eq. (7c), $D_{eff}^* = \varepsilon_f D_{eff} / \mathcal{D}_A$, ($D_{eff} = D_{eff}^*$ for an isotropic structure) and in Eq. (7a), φ is the Thiele modulus defined as

$$\varphi = \sqrt{\frac{Ki a_v^*}{D_{eff}^*}} \quad (8)$$

where Ki is the kinetic number

$$Ki = \frac{k_0 \alpha_A \ell_R}{\mathcal{D}_A} \quad (9)$$

152 4.1 Hybrid model

When $L_e^*/R_1^* \ll 1$, Eq. (7a) can be simplified to the following form

$$\frac{d^2 \langle c_A^* \rangle^f}{dr^{*2}} - \varphi^2 \langle c_A^* \rangle^f = 0, \quad R_1^* \leq r^* \leq R_2^* \quad (10)$$

In the absence of any other assumption (in particular if $L_e^* + L_N^*$ is not assumed to be exceedingly small compared to R_1^*), Eqs. (7b) to (7f) remain unchanged. This yields the hybrid model which solution is given by¹⁶

$$\langle c_A^* \rangle^f = a_1 \cosh(\varphi(r^* - R_1^*)) \quad R_1^* \leq r^* \leq R_2^* \quad (11a)$$

$$c_A^* = b_1 \ln r^* + c_1 \quad R_2^* \leq r^* \leq R_3^* \quad (11b)$$

with

$$a_1 = (\mathbf{D}_{eff}^* \varphi \sinh(\varphi L_e^*) R_2^* \ln(R_3^*/R_2^*) + \cosh(\varphi L_e^*))^{-1} \quad (12a)$$

$$b_1 = \left(\frac{\coth(\varphi L_e^*)}{\mathbf{D}_{eff}^* R_2^* \varphi} + \ln(R_3^*/R_2^*) \right)^{-1} \quad (12b)$$

$$c_1 = 1 - b_1 \ln(R_3^*) \quad (12c)$$

Moreover, the **current per unit volume** can be expressed as

$$\frac{I}{V_e} = - \frac{nFk_0 \alpha_A a_v c_A^0}{\varphi L_e^* [\coth(\varphi L_e^*) + \mathbf{D}_{eff}^* \varphi R_2^* \ln(R_3^*/R_2^*)]} \quad (13)$$

153 where V_e is the volume of the electrode immersed in the reactive solution, *i.e.*,
154 the active electrode volume.

155 4.2 Complete solution

156 At this point, no special hypothesis is made on the electrode dimensions and Eqs.
157 (7) are kept as such. The solution of Eq. (7a) is given by a linear combination
158 of the modified zeroth order Bessel's functions of the first and second kinds, I_0
159 and K_0 , as¹⁹

$$\langle c_A^* \rangle^f = A_1 I_0(\varphi r^*) + B_1 K_0(\varphi r^*), \quad R_1^* \leq r^* \leq R_2^* \quad (14)$$

160 The coefficients A_1 and B_1 can be determined by making use of the boundary
161 conditions (7c), (7d), (7e) and (7f). When this conditions are used, one obtains
162

$$A_1 = - \frac{K_1(\varphi R_1^*)}{I_1(\varphi R_1^*)} B_1 \quad (15a)$$

$$B_1 = \left[- \frac{K_1(\varphi R_1^*)}{I_1(\varphi R_1^*)} I_0(\varphi R_2^*) + K_0(\varphi R_2^*) + \mathbf{D}_{eff}^* \varphi R_2^* \ln \frac{R_3^*}{R_2^*} \left(- \frac{K_1(\varphi R_1^*)}{I_1(\varphi R_1^*)} I_1(\varphi R_2^*) - K_1(\varphi R_2^*) \right) \right]^{-1} \quad (15b)$$

163 where I_1 and K_1 are the first order modified Bessel's functions of the first and
 164 second kinds, respectively.

In the external diffusion layer, the concentration is given by

$$c_A^* = A_2 \ln r^* + B_2, \quad R_2^* \leq r^* \leq R_3^* \quad (16)$$

with

$$A_2 = \frac{1}{\ln(R_2^*/R_3^*)} (A_1 I_0(\varphi R_2^*) + B_1 K_0(\varphi R_2^*) - 1) \quad (17a)$$

$$B_2 = 1 - A_2 \ln R_3^* \quad (17b)$$

165 When the solution given in Eq.(14) is introduced in Eq. (6), **the current per**
 166 **unit active electrode volume**, V_e , takes the following expression

$$\begin{aligned} \frac{I}{V_e} &= -\frac{C}{R_2^{*2} - R_1^{*2}} \int_{R_1^*}^{R_2^*} [A_1 I_0(\varphi r^*) + B_1 K_0(\varphi r^*)] r^* dr^* \\ &= -\frac{C}{R_2^{*2} - R_1^{*2}} (A_1 F_1 + B_1 F_2) \end{aligned} \quad (18)$$

with C , F_1 and F_2 respectively given by

$$C = 2nk_0 F a_v \alpha_A c_A^0 \quad (19a)$$

$$F_1 = \int_{R_1^*}^{R_2^*} I_0(\varphi r^*) r^* dr^* = \frac{1}{\varphi} (R_2^* I_1(\varphi R_2^*) - R_1^* I_1(\varphi R_1^*)) \quad (19b)$$

$$F_2 = \int_{R_1^*}^{R_2^*} K_0(\varphi r^*) r^* dr^* = \frac{1}{\varphi} (R_1^* K_1(\varphi R_1^*) - R_2^* K_1(\varphi R_2^*)) \quad (19c)$$

167 In the following, numerical evaluation of the above solution on the **current**
 168 versus the scanning potential is compared to that of the hybrid model. The
 169 parameters used to compute these solutions are given in Table. 1. **They cor-**
 170 **respond to those used for the validation of the macroscopic model with direct**
 171 **numerical simulations of the microscale model and experimental data**^{13;14}. The
 172 electrochemical reaction considered here is typically the reduction of H_2O_2 to
 173 H_2O . Moreover, the face-centered cubic (FCC) structure is assumed as the pe-
 174 riodic REV of the porous medium constitutive of the electrode (see Fig. 2).
 175 This structure is uniquely defined by the sphere diameter, $d_s \equiv \ell_p$, and the pore
 176 connection window size, d_c ¹³. The REV of the FCC structure corresponds to 4
 177 half-layers (HL) of spherical pores.

178 The **current** versus the potential obtained from both the hybrid model and
 179 Bessel's solution is represented in Fig. 4(a) for three different electrodes made
 180 of 5HL, 15HL and 30HL of pores. As can be observed from this figure, the two
 181 solutions are almost identical when the potential is sufficiently large, although
 182 the hybrid model tends to underestimate the magnitude of the current. The
 183 discrepancy between the two models becomes significant below a threshold value
 184 of the potential which increases with the electrode thickness. This is made clear

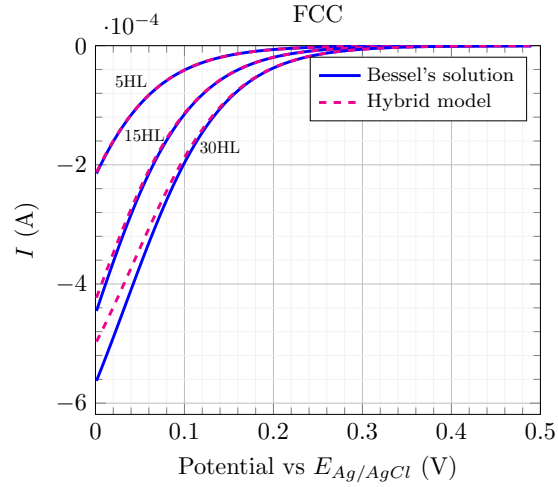
Table 1 – Parameters used for the solutions of the hybrid and complete models.

Parameter ^{13;14}	Symbol	Value	Unit
Ideal gas constant	R	8.314	J.mol ⁻¹ .K ⁻¹
Faraday’s constant	F	96485	C.mol ⁻¹
Number of electron transferred	n	2	–
Electron transfer coefficient	α	0.482	–
Standard rate constant	k_0	1.7×10^{-17}	cm.s ⁻¹
Standard potential vs. $E_{Ag/AgCl}^0$	E_0	1.56	V
Temperature	T	298	K
Bulk concentration	c_A^0	10	mol.m ⁻³
Diffusion coefficient	D_A	10^{-9}	m ² .s ⁻¹
Spherical pore diameter	$d_s = \ell_p$	1.17	μm
Pore connection window size	d_c	$0.15d_s$	m
Size of the periodic unit cell	ℓ_R	1.64	μm
Porosity	ε_f	0.763	–
Specific surface area	a_v	3.567×10^6	m ⁻¹
Normalized effective coefficient	D_{eff}^*	0.364	–
Wire radius	R_1	25	μm
Diffusion layer thickness	L_N	100	μm

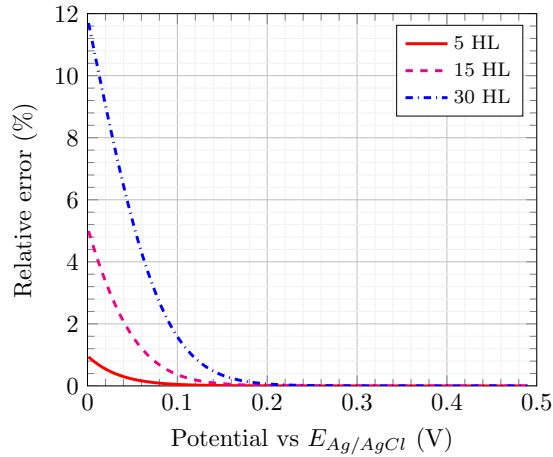
185 in Fig. 4(b) representing the absolute value of the relative error between the two
186 models (the Bessel’s solution is taken as the reference) showing that this relative
187 error can reach about 12 % for the thickest electrode under consideration when
188 the potential is close to 0V.

189 Numerical simulations on other microstructures, namely cubic (C) and body-
190 centered cubic (BCC) which unit cells are represented in Fig. 5, are also carried
191 out using the parameters given in Table 1. The resulting values of ε , a_v , D_{eff}^* and
192 ℓ_R are reported in Table 2. In Fig. 6, the **current** versus the scanning potential
193 obtained for different electrode thicknesses computed with the complete solution
194 and the hybrid model are represented for the C (Fig. 6(a)) and BCC (Fig. 6(b))
195 structures. As already observed for the FCC structure, a significant difference
196 between the two models exists in particular for a thick electrode, and this is a
197 general feature for any microstructure. Again, the hybrid model accuracy fails
198 when the thickness to inner radius ratio is not small enough compared to 1.

The analysis can now be focused on the optimal electrode thickness using the
same approach as the one recently investigated¹⁶. **To begin with, it is instructive
to illustrate the electrode efficiency with the reagent concentration profile. In
Fig. 7 $\langle c_A^* \rangle^f$ obtained from Eq. (14) with L_e^* and parameters of Table (1) is
represented within the electrode ($R_1^* < r^* < R_2^*$) for $Ki = 10^{-4}$ and $Ki = 10^{-3}$.
This figure clearly shows that the penetration depth of the concentration front
inside the electrode decreases as the kinetic number increases, *i.e.* when reaction
becomes more significant so that species *A* is consumed in the vicinity of the
electrode/diffusion layer interface. As a result, a large part of the electrode**



(a)



(b)

Figure 4 – (a) **Current** versus the scanning potential obtained from the hybrid model and Bessel's solution for the 5HL, 15HL and 30 HL electrodes. (b) Absolute value of the relative error between the two solutions taking the Bessel's solution as the reference.

(about half of it in Fig. 7 for $Ki = 10^{-3}$), in the region far enough from this interface, does not contribute much to the current production. This observation is an evidence that an optimal thickness can be determined and this is carried out as follows. The **current per unit volume** expressed in Eq. (18) decreases with the electrode thickness, L_e^* , in two characteristic regimes (see Fig. 8): a rapid decrease at small electrode thicknesses followed by a slow convergence to zero

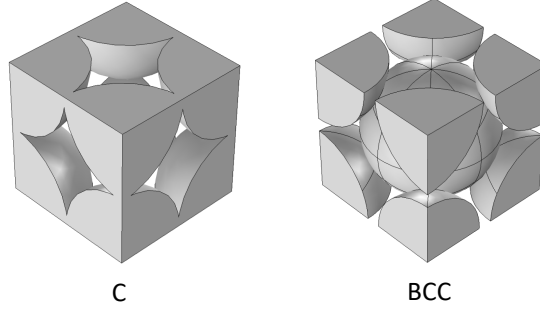


Figure 5 – Unit cell of the C and BCC structures.

Table 2 – Properties of C and BCC structures used in the simulations.

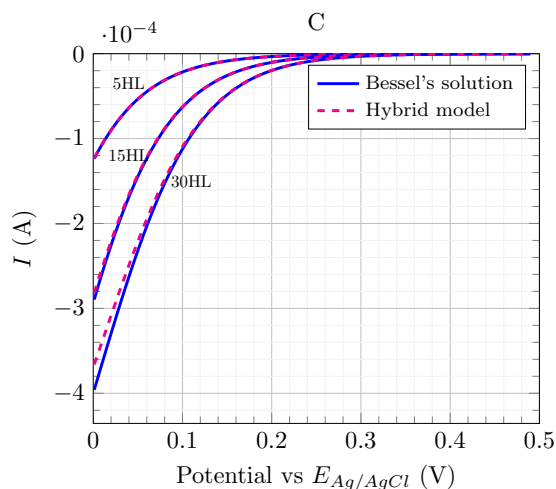
Parameter ¹³	Symbol	Value	Unit
C			
Porosity	ε_f	0.541	–
Specific surface area	a_v	2.68×10^6	m^{-1}
Normalized effective diffusion coefficient	D_{eff}^*	0.142	–
Size of the periodic unit cell	ℓ_R	1.16	μm
BCC			
Porosity	ε_f	0.703	–
Specific surface area	a_v	3.44×10^6	m^{-1}
Normalized effective diffusion coefficient	D_{eff}^*	0.236	–
Size of the periodic unit cell	ℓ_R	1.34	μm

at very large values of L_e^* . This suggests defining the optimal thickness, L_e^{*op} , as the crossover between these two regimes. Practically, this value is obtained at the intersecting point of the tangent to $|I/V_e|$ at L_e^{*0} with $|I/V_e|=0$. The value of L_e^{*0} should be taken as the minimum thickness that is experimentally achievable, *i.e.*, $L_e^{*0} \geq 1$. The value of L_e^{*op} can hence be obtained from the following expression

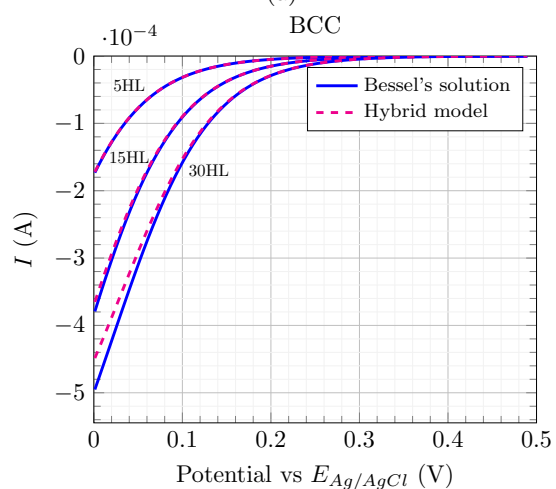
$$L_e^{*op} = - \frac{|I/V_e|_{L_e^{*0}}}{\left. \frac{\partial |I/V_e|}{\partial L_e^*} \right|_{L_e^{*0}}} + L_e^{*0} \quad (20)$$

The derivative of the **current per unit volume** with respect to L_e^* involved in this last relationship can be determined analytically from Eq. (18). It is given by

$$\frac{\partial(|I/V_e|)}{\partial L_e^*} = \frac{2R_2^*}{R_2^{*2} - R_1^{*2}} \frac{I}{V_e} + \frac{C}{R_2^{*2} - R_1^{*2}} \left(\frac{\partial A_1}{\partial L_e^*} F_1 + \frac{\partial B_1}{\partial L_e^*} F_2 + R_2^* \langle c_A^* \rangle^f \Big|_{R_2^*} \right) \quad (21)$$



(a)



(b)

Figure 6 – **Current** versus the scanning potential obtained from the hybrid model and Bessel's solution for the 5HL, 15HL and 30 HL electrodes: (a) cubic structure (C) (b) body-centered cubic structure (BCC).

199 As a result, the optimal electrode thickness can be estimated analytically once
 200 the electrode features are provided, namely ℓ_R , a_v^* , D_{eff}^* and R_1^* . Once these
 201 porous medium properties are fixed, the value of L_e^{*op} can be computed as it
 202 only depends on the conditions at which it is supposed to operate, *i.e.*, Ki
 203 and L_N^* . In the case of the FCC structure considered so far, and with the
 204 parameters reported in Table 1, together with $L_e^{*0} = 1$, L_e^{*op} was computed

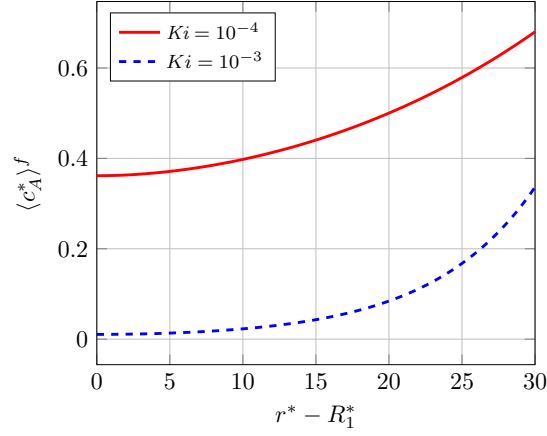


Figure 7 – Normalized concentration profile of species A in the electrode for two values of the kinetic number. The dimensionless electrode thickness is $L_e^* = 30$ the other parameters being those in Table 1.

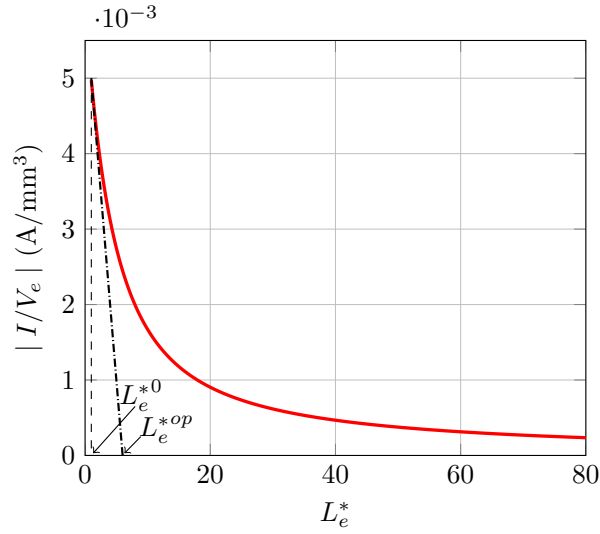


Figure 8 – Variation of the **current per unit volume**, $|I/V_e|$, obtained from Eq. (18) versus the electrode's dimensionless thickness, L_e^* , in the case of a FCC microstructure for $Ki = 10^{-3}$ and $L_N = 100\mu\text{m}$. The other parameters used to compute the **current per unit volume** are provided in Table 1. **The optimal thickness**, L_e^{*op} , is obtained from the intersection of the tangent to this graph at $L_e^* = L_e^{*0}$ with the axis $|I/V_e| = 0$. See text for the details.

205 from Eq. (20) for Ki values up to 2×10^{-3} . The corresponding results are
 206 reported in Fig. 9(a) considering two values of the diffusion layer thickness,

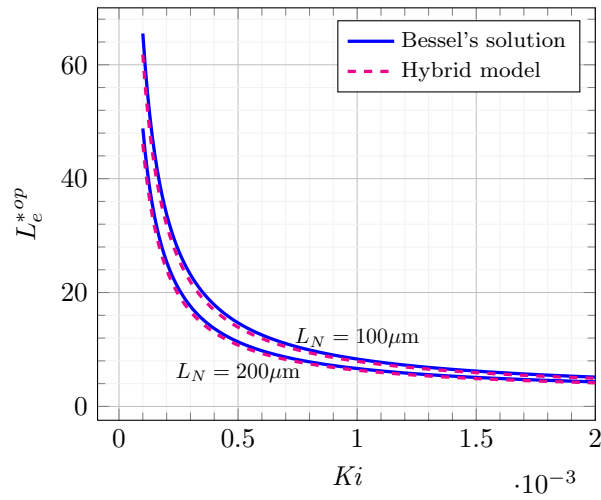
207 namely $L_N = 100\mu\text{m}$ and $L_N = 200\mu\text{m}$. As expected, L_e^{*op} increases when L_N
 208 decreases. This is due to the fact that a thinner diffusion layer (*i.e.* imposing
 209 a Dirichlet boundary condition closer to the fluid porous layer interface) allows
 210 a more efficient penetration of the reagent inside the porous electrode so that
 211 a thicker active layer is permitted. In addition, the optimal thickness obtained
 212 with the hybrid model reported elsewhere¹⁶ is also represented in this figure.

213 As can be observed on this figure, the difference between the predictions of
 214 the two models remains very small. This is highlighted in Fig. 9(b) representing
 215 the relative error between the two predictions, taking the Bessel's solution as
 216 the reference. Indeed, the largest difference is for the smallest values of Ki (*i.e.*
 217 for the largest values of E) and small values of the diffusion layer thickness. For
 218 the case under study, this difference does not exceed 6%.

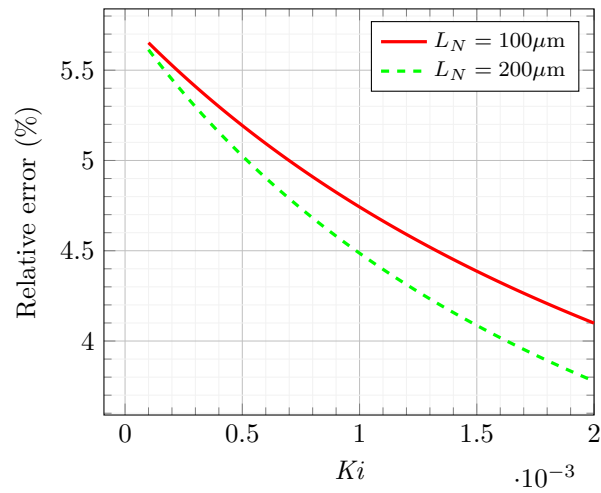
219 These results show that the hybrid model remains robust if one is willing
 220 to estimate the optimal thickness of the electrode although it can significantly
 221 underestimate the **current**, in particular for the smallest values of the potential
 222 when the condition $2L_e^*/(R_1^* + R_2^*) \ll 1$ is not satisfied.

223 The normalized optimal thickness predicted for the other microstructures (C
 224 and BCC), compared to the FCC structure, is represented in Fig. 10. Clearly,
 225 the dependence of L_e^{*op} on Ki is similar whatever the structure. This brings to
 226 the general conclusion that, whatever the microstructure, the optimal thickness
 227 decreases rapidly with the kinetic number and tends to a constant value for large
 228 values of Ki . Quantitatively, the comparison of the optimal thickness of the three
 229 structures must be made with care as L_e^{*op} and Ki are based on ℓ_R which is not
 230 the same from one structure to another. For this purpose, a representation
 231 where $\ell_p = d_s$ (identical for C, BCC and FCC) is used as the reference length is
 232 given in the inset of Fig. 10. It shows that the optimal thickness for the BCC
 233 and FCC structures is almost the same (it is slightly larger for the former),
 234 but is larger for the C structure. The physical explanation of this behavior
 235 can be deduced after examining the reduced sensibility of L_e^{*op} to a_v and D_{eff}^*
 236 that are reported in Fig. 11. It should be noted that the reduced sensibility of
 237 L_e^{*op} to the parameter u is defined as $u\partial L_e^{*op}/\partial u$. This figure shows that the
 238 reduced sensibility to a_v is negative (*i.e.* L_e^{*op} increases when a_v decreases) and
 239 is much larger in magnitude than that to D_{eff}^* . Consequently, the contrast on
 240 L_e^{*op} between the three structures can be interpreted only considering a_v . Since
 241 a_v is not markedly different for the BCC and FCC structures (although slightly
 242 smaller for the former) but significantly smaller for the C structure (see Tables
 243 1 and 2), the expected variation of L_e^{*op} with respect to the structure is exactly
 244 that observed in Fig. 10 and mentioned above.

245 Finally, it is of interest to investigate which structure, among the three
 246 considered here, is the most efficient in terms of current production. Results
 247 of the current per unit length, L , of the electrode at its optimal thickness are
 248 represented in Fig. 12 for the C, BCC and FCC structures versus Ki . From
 249 this figure, it can readily be concluded that the FCC structure produces the largest
 250 current per unit length. In addition to the fact that it also allows the thinner
 251 optimal thickness, this structure is the most advantageous one among the three
 252 simple cases envisaged here. In what follows, results are only illustrated for a



(a)



(b)

Figure 9 – (a) Optimal thickness versus the kinetic number for two values of the diffusion layer thickness, obtained from the Bessel’s solution and hybrid model (b) Absolute relative error between the two approaches taking the values obtained with the Bessel’s solution as the reference. FCC structure. Parameters are those reported in Table 1.

253 FCC structure.

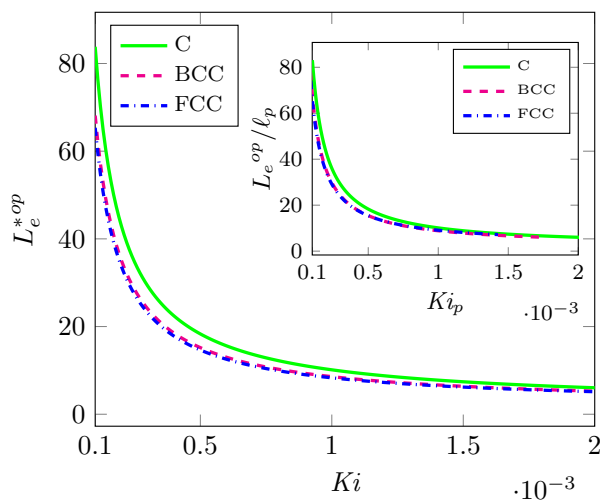


Figure 10 – Optimal thickness versus the kinetic number for C, BCC and FCC structures. $L_N = 100\mu\text{m}$. For all structures, d_c and d_s are the same (see Table 1) featuring different values of ε , a_v , D_{eff}^* and ℓ_R (see the values in Table 1 for the FCC and in Table 2 for the C and BCC structures respectively). All other parameters are the same and are reported in Table 1. Inset: L_e^{*op} made dimensionless by the spherical pore diameter, $\ell_p = d_s$, versus the pore kinetic number, $Ki_p = \frac{k_0\alpha_A\ell_p}{D_A}$ for the three structures.

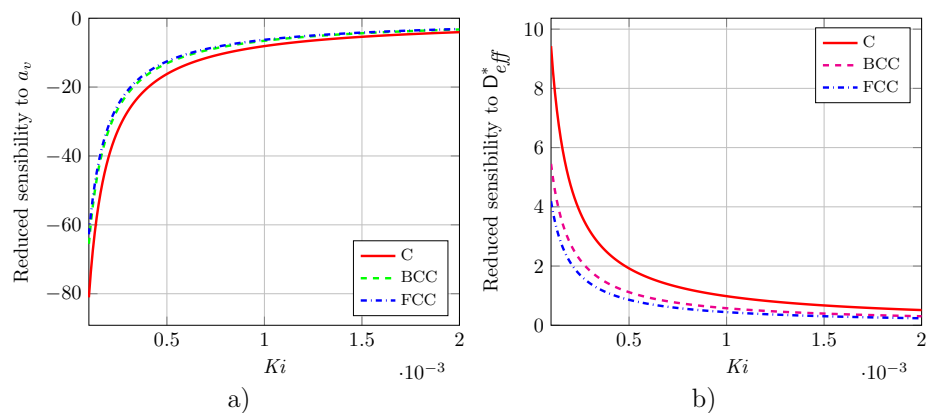


Figure 11 – Reduced sensibility of L_e^{*op} to a) a_v and b) D_{eff}^* for the three structures C, BCC and FCC.

254 5 Planar electrode

For the sake of completeness, the case of a planar electrode is now investigated by providing the analytical solution for the current and optimal thickness. In this

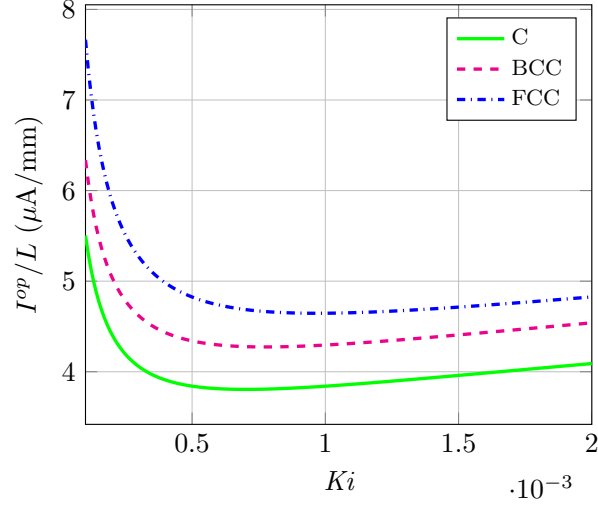


Figure 12 – Current per unit length, L , of the electrode at its optimal thickness for the three structures C, BCC and FCC versus Ki . Parameters are those reported in Table 1.

situation, the porous material is deposited onto a plane solid surface, as in the cases envisaged by Barnes *et al.*² and Cai *et al.*⁴, for instance. Assuming that the extension of the electrode in both directions of the plane are much larger than the electrode thickness, the model reduces to one dimension, in the z -direction orthogonal to the plane. Using the same dimensionless variables as in section 4, the problem can be formulated as follows

$$\frac{\partial^2 \langle c_A^* \rangle^f}{\partial z^{*2}} - \varphi^2 \langle c_A^* \rangle^f = 0 \quad 0 \leq z^* \leq L_e^* \quad (22a)$$

$$\frac{\partial}{\partial z^*} \left(\frac{\partial c_A^*}{\partial z^*} \right) = 0 \quad L_e^* \leq z^* \leq L_e^* + L_N^* \quad (22b)$$

$$\text{B.C.1} \quad \frac{\partial \langle c_A^* \rangle^f}{\partial z^*} = 0 \quad z^* = 0 \quad (22c)$$

$$\text{B.C.2} \quad \langle c_A^* \rangle^f = c_A^* \quad z^* = L_e^* \quad (22d)$$

$$\text{B.C.3} \quad D_{eff}^* \frac{\partial \langle c_A^* \rangle^f}{\partial z^*} = \frac{\partial c_A^*}{\partial z^*} \quad z^* = L_e^* \quad (22e)$$

$$\text{B.C.4} \quad c_A^* = 1 \quad z^* = L_e^* + L_N^* \quad (22f)$$

The analytical solution to the above system of equations is given by

$$\langle c_A^* \rangle^f = a_2 \cosh(\varphi z^*) \quad 0 \leq z^* \leq L_e^* \quad (23a)$$

$$c_A^* = b_2 z^* + c_2 \quad L_e^* \leq z^* \leq L_e^* + L_N^* \quad (23b)$$

where the coefficients a_2 , b_2 and c_2 have the following expressions

$$a_2 = [\cosh(\varphi L_e^*) + D_{eff}^* \varphi L_N^* \sinh(\varphi L_e^*)]^{-1} \quad (24a)$$

$$b_2 = \left[\frac{\coth(\varphi L_e^*)}{D_{eff}^* \varphi} + L_N^* \right]^{-1} \quad (24b)$$

$$c_2 = 1 - b_2(L_e^* + L_N^*) \quad (24c)$$

Using Eq. (23a) in Eq. (6), the **current** per unit volume, V_e , can be written as

$$I/V_e = - \frac{nFk_0\alpha_A a_v c_A^0}{\varphi L_e^* [\coth(\varphi L_e^*) + D_{eff}^* \varphi L_N^*]} \quad (25)$$

Its derivative with respect to L_e^* can then be expressed as

$$\frac{\partial |I/V_e|}{\partial L_e^*} = - \frac{nFk_0\alpha_A a_v c_A^0}{\varphi} \frac{\varphi(1 - \coth^2(\varphi L_e^*))L_e^* + \coth(\varphi L_e^*) + D_{eff}^* \varphi L_N^*}{[\coth(\varphi L_e^*)L_e^* + D_{eff}^* \varphi L_N^* L_e^*]^2} \quad (26)$$

255 From these two last relationships, the optimal thickness can be determined
 256 by making use of Eq. (20). The results of this prediction is represented in Fig.
 257 13 considering a FCC structure, $L_N = 100\mu\text{m}$, $L_e^{*0} = 1$ and Ki up to 2×10^{-3} ,
 all the other parameters being those reported in Table 1. As a validation,

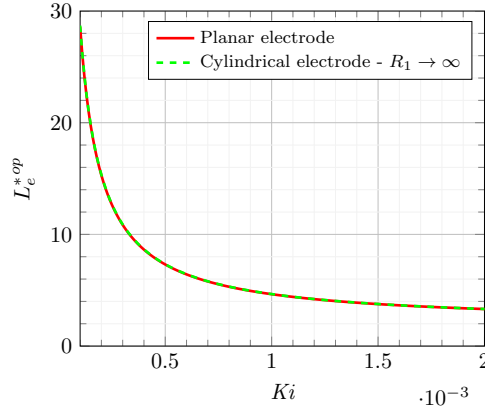


Figure 13 – Optimal thickness versus the kinetic number obtained for planar electrode and cylindrical electrode taking $R_1 \rightarrow \infty$. $L_N = 100\mu\text{m}$. FCC structure. All the parameters are those reported in Table 1.

258 the solution of the complete model in the limit $R_1 \rightarrow \infty$ is also reported in
 259 this figure, showing that, in this limit, the two predictions perfectly match, as
 260 expected. This confirms that the complete solution is a general one, whatever
 261 the electrode dimensions. On the basis of this general result, the analysis can
 262 be carried on to determine the optimal radius, R_1^{*op} , of the supporting wire and
 263 this is the objective of the following section.
 264

265 **6 Optimal wire radius, R_1^{*op}**

266 A comparison of the results reported in Fig. 13 with those in Fig. 9(a) indicates
 267 that, all parameters being the same, the optimal thickness of the planar electrode
 268 is smaller than that of a cylindrical electrode having a finite radius. The contrast
 269 between the two is more significant when Ki decreases. This suggests to further
 270 analyze the dependence of L_e^{*op} upon the wire radius, R_1^* , for a given set of the
 271 physico-chemical parameters. More particularly, it is of interest to investigate
 272 the variation of the volume (per unit length, L) of the electrode at its optimal
 273 thickness, V_e^{op}/L , with respect to R_1^* . Such a variation is illustrated in Fig.
 274 14, considering two values of Ki , namely $Ki = 5 \cdot 10^{-4}$ and $Ki = 10^{-3}$, taking
 275 $L_N = 100\mu\text{m}$, all other parameters being those reported in Table 1 and a FCC
 structure.

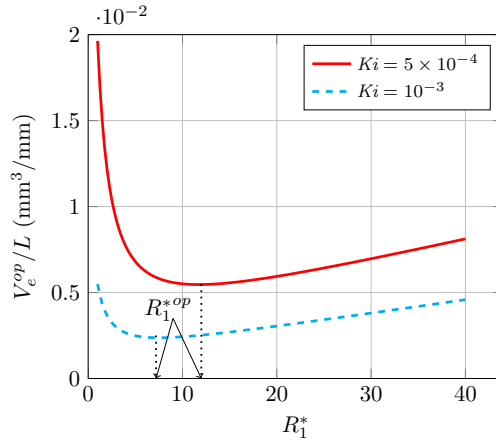


Figure 14 – Variation of the volume (per unit length, L) of the electrode at its optimal thickness, V_e^{op}/L , versus the dimensionless wire radius, R_1^* , for $Ki = 5 \cdot 10^{-4}$ and $Ki = 10^{-3}$, taking $L_N = 100\mu\text{m}$ (see Table 1 for the other parameters). FCC structure.

276
 277 This figure clearly shows that V_e^{op}/L exhibits a minimum which means that
 278 there exists a particular value of R_1^* , denoted R_1^{*op} , which minimizes the volume
 279 of material necessary to achieve the optimal thickness. This is extremely im-
 280 portant keeping in mind that the porous medium is usually made of expensive
 281 materials using complex procedures. In Fig. 15, R_1^{*op} is represented versus Ki
 282 in the range $10^{-4} \leq Ki \leq 10^{-3}$ for $L_N = 100\mu\text{m}$. As can be seen on this graph,
 283 the optimal wire radius decreases when Ki increases. Moreover, R_1^{*op} seems to
 284 very weakly depend on L_N , as indicated by Fig. 16 where R_1^{*op} is represented
 285 versus L_N ranging from $100\mu\text{m}$ to $400\mu\text{m}$ for $Ki = 5 \cdot 10^{-4}$ and $Ki = 10^{-3}$. This
 286 suggests that the value of R_1^{*op} can be determined regardless the value of L_N ,
 287 *i.e.* as only a function of Ki when the microstructural parameters are fixed.

288 This last analysis completes the optimization procedure of the electrode

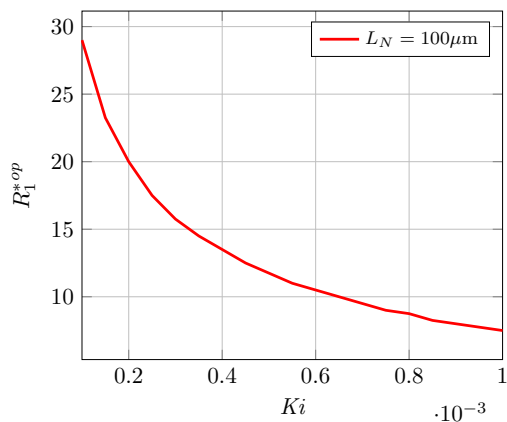


Figure 15 – Variation of the dimensionless optimal wire radius, R_1^{*op} , versus Ki for $L_N = 100\mu\text{m}$ (see Table 1 for the other parameters). FCC structure.

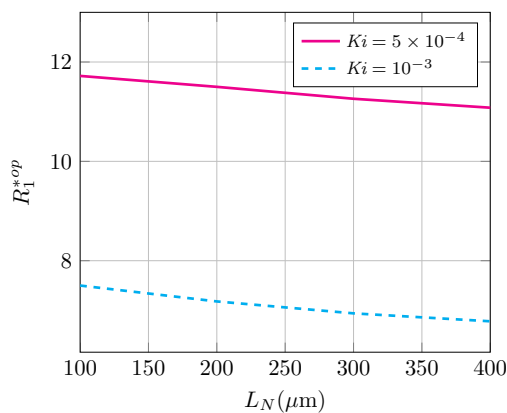


Figure 16 – Variation of the dimensionless optimal wire radius, R_1^{*op} , versus L_N for $Ki = 5 \cdot 10^{-4}$ and $Ki = 10^{-3}$ (see Table 1 for the other parameters). FCC structure.

289 macroscopic dimensions as its thickness and supporting wire diameter can be
 290 predicted in order to obtain the optimal current **per unit volume** when the
 291 operating conditions and the microstructure of the porous material are known.
 292 This represents a major result of this work.

293 7 Conclusion

294 In this work, steady-state solutions of the macroscopic model describing the
 295 coupled process of electrochemical heterogeneous reaction and diffusion are de-
 296 veloped for cylindrical and planar porous micro-electrodes.

297 The complete solution developed here provides a more accurate prediction
298 of the current delivered by the electrode versus the applied potential than the
299 hybrid model reported earlier which is recovered in the limit of a thickness to
300 inner radius ratio much smaller than unity and which remains valid in this
301 limit. Moreover, the complete solution also matches the one developed in the
302 case of a planar electrode in the limit of exceedingly large radii. This makes the
303 complete solution a general one, whatever the dimensions and microstructure
304 of the electrode, **the characteristics of the latter being reflected in the porosity,**
305 **specific area and effective diffusion coefficient. The use of this complete solution**
306 **is strongly recommended particularly when the constraint on the dimensions is**
307 **not satisfied.**

308 More importantly, it is shown that an optimal radius of the supporting wire
309 exists for a given set of the physico-chemical parameters defining the operating
310 conditions of the electrode. This optimal radius is derived as to satisfy the
311 minimum volume of the porous material required to ensure the optimal **current**
312 **per unit volume.** This represents a salient result of the present work.

313 Together with the prediction of the current delivered by the electrode, the
314 solution derived here allows for the determination of the electrode optimal di-
315 mensions in terms of its thickness and inner radius. This provides a complete
316 and effective operational procedure of optimization of the macroscopic char-
317 acteristics of cylindrical electrodes operating a single reduction reaction as a
318 predictive tool for their practical design. **As a final remark, it should be noticed**
319 **that the approach developed here may be advantageously employed for the opti-**
320 **mal design of other electrochemical devices devoted to energy production which**
321 **architecture and operating share similarities with those envisaged in this work.**

322 8 Acknowledgment

323 This work was supported by the ANR project MOMA (ANR-17-CE08-0005).

324 9 Keywords

325 Porous micro-electrode, Optimal thickness, Optimal radius, Analytical solution,
326 Volume averaging method

327 References

- 328 [1] Barcia, O.E., D’Elia, E., Frateur, I., Mattos, O.R., Pebere, N., Tribollet,
329 B., 2002. Application of the impedance model of de Levie for the charac-
330 terization of porous electrodes. *Electrochimica Acta* 47, 2109–2116.
- 331 [2] Barnes, E.O., Chen, X., Li, P., Compton, R.G., 2014. Voltammetry at
332 porous electrodes: A theoretical study. *Journal of Electroanalytical Chem-*
333 *istry* 720–721, 92–100.

- 334 [3] Butler, J.A.V., 1924. Studies in heterogeneous equilibria. part ii. the kinetic
335 interpretation of the nernst theory of electromotive force. Transactions of
336 the Faraday Society 19, 729–733.
- 337 [4] Cai, Q., Adjiman, C.S., Brandon, N.P., 2011. Investigation of the active
338 thickness of solid oxide fuel cell electrodes using a 3d microstructure model.
339 Electrochim. Acta 56, 10809–10819.
- 340 [5] Cosnier, S., Gross, A.J., Goff, A.L., Holzinger, M., 2016. Recent advances
341 on enzymatic glucose/oxygen and hydrogen/oxygen biofuel cells: Achieve-
342 ments and limitations. Journal of Power Sources 325, 252–263.
- 343 [6] Do, T.Q.N., Varničić, M., Flassig, R., Vidaković-Koch, T., Sundmacher, K.,
344 2015. Dynamic and steady state 1-D model of mediated electron transfer
345 in a porous enzymatic electrode. Bioelectrochemistry 106, 3–13.
- 346 [7] Do, T.Q.N., Varničić, M., Hanke-Rauschenbach, R., Vidaković-Koch, T.,
347 Sundmacher, K., 2014. Mathematical modeling of a porous enzymatic elec-
348 trode with direct electron transfer mechanism. Electrochimica Acta 137,
349 616–626. doi:10.1016/j.electacta.2014.06.031.
- 350 [8] Fick, A., 1995. On liquid diffusion. Journal of Membrane Science 100,
351 33–38.
- 352 [9] Gamella, M., Koushanpour, A., Katz, E., 2018. Biofuel cells - Activation
353 of micro- and macro-electronic devices. Bioelectrochemistry 119, 33–42.
- 354 [10] Gray, W., 1975. A derivation of the equations for multiphase transport.
355 Chem. Eng. Sci. 30, 229–233. doi:10.1016/0009-2509(75)80010-8.
- 356 [11] Howes, F., Whitaker, S., 1985. The spatial averaging theorem revisited.
357 Chem. Eng. Sci. 40, 1387–1392. doi:10.1016/0009-2509(85)80078-6.
- 358 [12] Karajić, A., Reculosa, S., Heim, M., Garrigue, P., Ravaine, S., Mano,
359 N., Kuhn, A., 2015. Bottom-up generation of miniaturized coaxial double
360 electrodes with tunable porosity. Advanced Materials Interfaces 2, 1500192–
361 1500196. doi:10.1002/admi.201500192.
- 362 [13] Le, T.D., Lasseux, D., Nguyen, X.P., Vignoles, G.L., Mano, N., Kuhn, A.,
363 2017. Multi-scale modeling of diffusion and electrochemical reactions in
364 porous micro-electrodes. Chemical Engineering Science 173, 153–167.
- 365 [14] Le, T.D., Zhang, L., Gounel, S., Mano, N., Kuhn, A., Lasseux, D., 2019a.
366 Multiscale modelling of diffusion and enzymatic reaction in porous elec-
367 trodes in Direct Electron Transfer mode. To appear in Electrochimica
368 Acta .
- 369 [15] Le, T.D., Zhang, L., Kuhn, A., Mano, N., Vignoles, G.L., Lasseux, D.,
370 2019b. Upscaled model for diffusion and serial reduction pathways in porous
371 electrodes. Journal of Electroanalytical Chemistry 855, 113325. doi:10.
372 1016/j.jelechem.2019.113325.

- 373 [16] Le, T.D., Zhang, L., Vignoles, G.L., Mano, N., Kuhn, A., Lasseux, D.,
374 2019c. Optimal thickness of a porous micro-electrode operating a single
375 redox reaction. *ChemElectroChem* 6, 173–180.
- 376 [17] Leech, D., Kavanagh, P., Schuhmann, W., 2012. Enzymatic fuel cells:
377 Recent progress. *Electrochimica Acta* 84, 223–234.
- 378 [18] Levie, R.D., 1967. Electrochemical response of porous and rough electrodes.
379 *Advances in Electrochemistry and Electrochemical Engineering* 6, 329–397.
- 380 [19] Polyanin, A.D., Zaitsev, V.F., 2003. *Handbook of Exact Solutions for*
381 *Ordinary Differential Equations*. Chapman and Hall/CRC, 3rd Ed.
- 382 [20] Reculosa, S., Heim, M., Gao, F., Mano, N., Ravaine, S., Kuhn, A., 2011.
383 Design of catalytically active cylindrical and macroporous gold microelec-
384 trodes. *Advanced Functional Materials* 21, 691–698. doi:10.1002/adfm.
385 201001761.
- 386 [21] Shleev, S., 2017. Quo vadis, implanted fuel cell? *ChemPlusChem* 82,
387 522–539.
- 388 [22] Slattery, J.C., 1999. *Advanced Transport Phenomena (Cambridge Se-*
389 *ries in Chemical Engineering)*. Cambridge University Press. URL:
390 www.cambridge.org/9780521635653.
- 391 [23] Walcarius, A., Kuhn, A., 2008. Ordered porous thin films in electrochemical
392 analysis. *Trends in Analytical Chemistry* 27, 593–603.
- 393 [24] Whitaker, S., 1999. *The Method of Volume Averaging*. Kluwer Academic
394 Publishers, Dordrecht, The Netherlands.
- 395 [25] Whitaker, S., 2009. Derivation and application of the Stefan-Maxwell equa-
396 tions. *Revista Mexicana de Ingenieria Quimica* 8, 213–243.
- 397 [26] Zebda, A., Alcaraz, J., Vadgama, P., Shleev, S., Minteer, S.D., Boucher,
398 F., Cinquin, P., Martin, D.K., 2018. Challenges for successful implantation
399 of biofuel cells. *Bioelectrochemistry* 124, 57–72.